Journal of Materials Chemistry B

Accepted Manuscript

ROYAL SOCIETY OF CHEMISTRY

www.rsc.org/materialsB

Journal Name

RSCPublishing

ARTICLE

An Upconversion Nanoprobe Operating in the First Biological Window

Cite this: DOI: 10.1039/x0xx00000x

Qiang Ju,[a] Xian Chen,[a] Fujin Ai,[b] Dengfeng Peng,[a] Xudong Lin,[c] Wei Kong,[a] Peng Shi,[c,d] Guangyu Zhu,[b,d] and Feng Wang[a,d]*

Received 00th January 2012,
Accepted 00th January 2012

DOI: 10.1039/x0xx00000x

www.rsc.org/

Upconversion nanoparticles capable of converting low-energy excitation into higher-energy emission have been proved useful for sensitive biodetection due to the largely eliminated background autofluorescence and light scattering effects. However, the existing techniques have been constrained due to the absorption of excitation and emission light by water and hemoglobin in biological settings that typically result in low light penetration depth and potential thermal damage to biological samples. In this work, a core−shell−shell nanostructure is described to realize photon upconversion in the first biological spectral window (650−900 nm) where the absorption of water and biological specimen is minimal. We synthesized core−shell−shell nanoparticles with small feature size (~30 nm) that display dominant emission in the far red (660 nm) spectral region on excitation at 808 nm. The as-synthesized core−shell−shell nanoparticles were further developed as optical bioprobes that offer sensitive biodetection in the presence of tissue wrapping.

Introduction

The development of luminescent bioprobes has enabled precise decipherment of chemical information and rapid molecular detection in complex biological systems.[1] Luminescent bioprobes with the emission and excitation both located in the first biological window (i.e., ~650–900 nm) are particularly useful for biological research and biomedical applications, attributed to the minimal light absorptions by hemoglobin and water components in biological tissues within this spectral region (Figure S1).[2] In principle, optical imaging and detection operating in the biological window can achieve high tissue penetration depth along with largely eliminated photo-toxicity or overheating effect associated with the irradiation light. However, spectral conversions in the range of far red to near infrared (NIR) typically involves the use of organic dyes or quantum dots. These systems suffer from several intrinsic problems including poor photochemical stability and high long-term toxicity, thus posing limitations in practical applications.

As an attractive alternative to organic dyes and quantum dots, lanthanide-doped nanoparticles have been developed as a new class of luminescent bioprobes that are characterized by narrow emission bandwidths (<20 nm), reduced long-term toxicity to tissue, and high resistance to optical blinking and photochemical degradation.[3] In addition, lanthanide-doped nanoparticles can convert low-energy excitation radiation into higher-energy emissions through a unique photon upconversion process.[4] The effect has been proven useful to increase detection sensitivity and to improve imaging contrast by eliminating background autofluorescence inevitably accompanying the use of Stokes-shifting biolabels.[5] Particularly, lanthanide ions featuring enormously complex energy levels can result in a wealth of optical transitions. Uniting different lanthanide ions by means of energy transfer can give rise to highly designable upconversion processes, provided that the nonradiative deactivation is largely eliminated.[6]

Recently, several attempts have been made to optimize the upconversion properties for biomedical applications by taking advantage of nanostructural engineering to integrate incompatible lanthanide ions. For example, core−shell nanoparticles have emerged as a new platform to integrate incompatible lanthanide ions for creating new upconversion properties, which has expedited the development of Nd^{3+}-sensitized upconversion featuring an excitation maximum at ~800 nm. Excitation with 800 nm laser typically avoids sample overheating in biological systems owing to the reduced light absorption by water.[7] However, most of the Nd^{3+}-sensitized upconversion nanoparticles displays dominant emission bands in the blue and green spectral regions, which are not clinically preferred

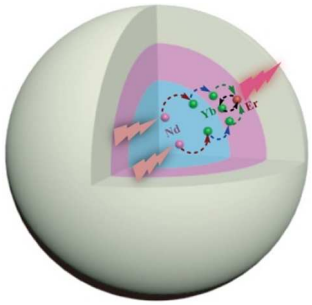

Fig. 1 Schematic design of the core−shell−shell nanoparticles for performing upconversion in the medical transparent windows. The core and shell layers are highlighted with different background colours. Nd^{3+} is doped in the core layer to harvest the NIR excitation light at 808 nm. Er^{3+} in the inner shell layer is used to convert excitation light into 660-nm emission through the $^4F_{9/2} \rightarrow {}^4I_{15/2}$ transition. The outermost $NaGdF_4$ shell is designed to protect the upconversion process against surface quenching.

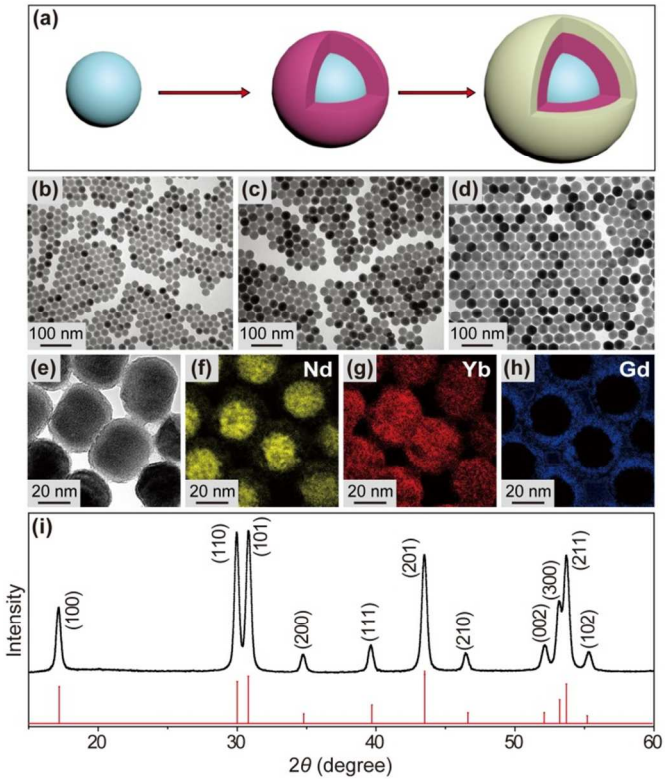

Fig. 2 Synthesis and characterization of the core–shell–shell nanoparticles. (a) Schematic illustration for the layer-by-layer growth process. (b–d) TEM images of the $NaYbF_4$:Nd (45 mol %) core, the $NaYbF_4$:Nd@$NaGdF_4$:Yb/Er (78/2 mol %) core–shell, and the $NaYbF_4$:Nd@$NaGdF_4$:Yb/Er@$NaGdF_4$ core–shell–shell nanoparticles, respectively. (e) TEM image of randomly selected nanoparticles for compositional analysis. (f–g) Element maps of Nd, Yb, and Gd in the nanoparticles shown in (e). (i) XRD pattern of the core–shell–shell nanoparticle and the corresponding line pattern of hexagonal phase $NaYbF_4$ (JCPDS standard card no. 27-1427).

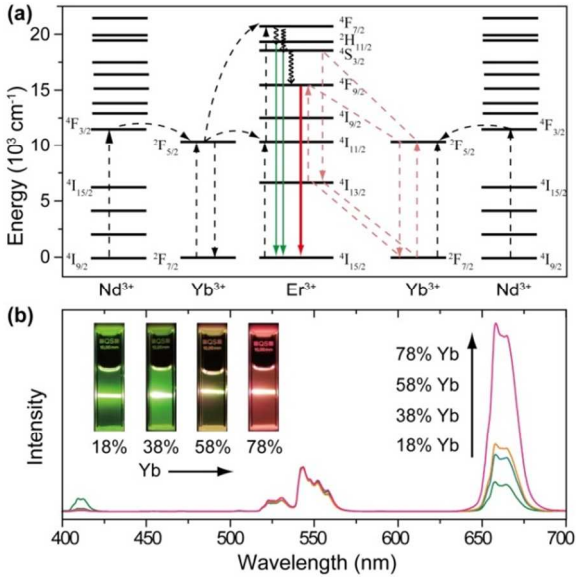

Fig. 3 Optimization of the red upconversion emission of Er^{3+}. (a) Proposed energy transfer mechanism that facilitates red upconversion emission of Er^{3+} after excitation into Nd^{3+}. (b) Emission spectra of the $NaYbF_4$:Nd@$NaGdF_4$:Yb/Er@$NaGdF_4$ core–shell–shell nanoparticles as a function of Yb^{3+} concentration in the inner shell layer. The spectra were normalized to the green emission band of Er^{3+} at 542 nm. Inset: luminescence photographs of the corresponding nanoparticle colloids.

due to attenuation of the emission light by biological samples. Herein, we describe a core–shell–shell nanoparticle platform for independent tuning of the excitation and emission spectra of upconversion nanoparticles. We synthesize quasi-spherical core–shell–shell nanoparticles featuring small particle size (~30 nm) and high dopant concentration of Yb^{3+} (78 mol%). We demonstrate that the nanoparticles display dominant emission at 660 nm in biological settings by 808-nm excitation, offering sensitive detection of single-strand DNAs and cancer cells in the presence of tissue wrapping.

We chose to realize the desired upconversion property in a $NaYbF_4$:Nd@$NaGdF_4$:Yb/Er@$NaGdF_4$ core–shell–shell nanoparticle (Figure 1). Nd^{3+} and Er^{3+} are confined in separate layers to avoid nonradiative deactivations. Yb^{3+} network across the core–shell interface are designed to initiate $Nd^{3+} \rightarrow Yb^{3+} \rightarrow Er^{3+}$ energy transfer and to tune the optical emission of Er^{3+} through $Er^{3+} \rightarrow Yb^{3+}$ back-energy-transfer. Notably, in previous studies on Nd^{3+}-sensitized upconversion core–shell nanoparticles the activator ions (i.e., Er^{3+}) are typically encoded in the core layer.[7a, c] To retain a relatively small particle size that is essential for facilitating interlayer energy transfers, the Yb^{3+} content in the core layer should be carefully designed (Figure S2), which imposes serious constraints on tuning the emission spectra. Our strategy alleviates this limitation by composing the Er^{3+}-doped upconversion layer on Nd^{3+}-doped core nanoparticles featuring small particle size (Figure S2), which can serve as a template to direct the growth of consistent shells essentially irrespective of the shell composition.[8] As an added benefit, Er^{3+} ions in the peripheral region of the nanoparticle are likely to donate their energy to optical centers in close proximity to the nanoparticle surface, thereby facilitating homogenous biological detection (vide infra).[9]

Results and discussion

The nanoparticles were synthesized through successive deposition of $NaGdF_4$:Yb/Er and $NaGdF_4$ shell layers on pre-synthesized $NaYbF_4$:Nd (45 mol %) cores (Figure 2a).[8] The relatively low Nd^{3+} content (45 mol %) with respect to previous study (50 mol %)[7b] was found to suppress nonisotropic shell growth during the epitaxial coating process, probably due to reduced variations in surface energies of different facets. Transmission electron microscopy (TEM) images reveal quasi-spherical shape of the as-synthesized core nanoparticles with a main particle size of 22±1.8 nm (Figure 2b). Typical core–shell (Figure 2c) and core–shell–shell (Figure 2d) nanoparticles obtained by successive coating of $NaGdF_4$:Yb/Er (78/2 mol %) and $NaGdF_4$ layers closely resemble the morphology of the core nanoparticle with narrow size distributions (27±2.5 nm and 31±2.2 nm), suggesting a fairly uniform shell deposition process. The electron energy loss spectroscopy (EELS) analysis illustrates that the elemental distributions of the nanoparticles are very consistent with the designed compositions (Figure 2e–h), confirming the core–shell–shell structure of the nanoparticles. The as-synthesized nanoparticles display much stronger emission than the homogeneously doped counterparts (Figure S3), further validating the formation of core–shell–shell structures that eliminate deleterious cross-relaxations. The highly crystalline nature of core–shell–shell nanoparticles was confirmed by X-ray powder diffraction (XRD)

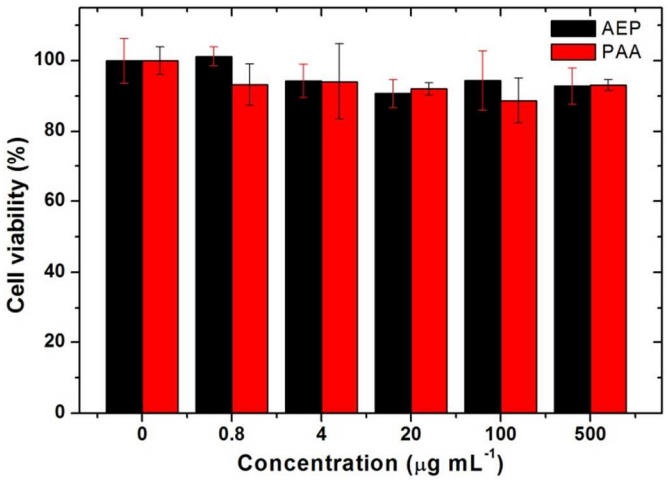

Fig. 4 *In-vitro* cytotoxicity of the AEP- and PAA-capped core−shell−shell nanoparticles against *KB cells* after 24-hr incubation.

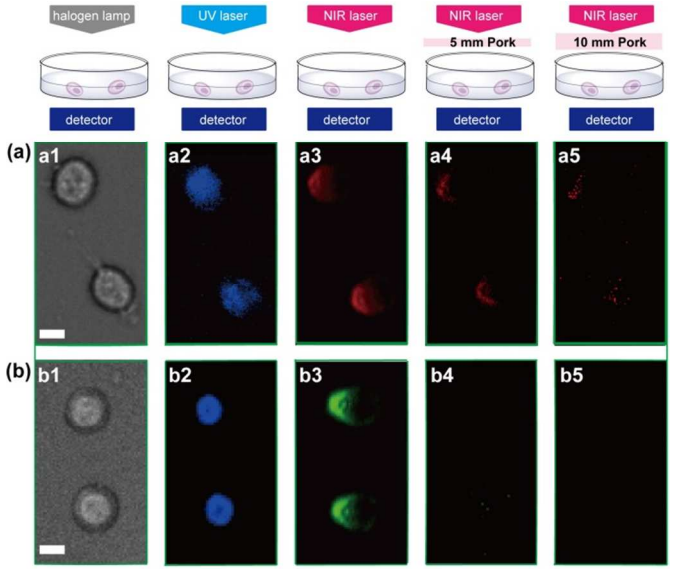

Fig. 5 Cellular detection with the upconversion nanoparticles. (a, b) Optical micrographs of *KB cells* (100 μg/mL) after a 4-hr incubation with the FA-conjugated 808-to-660 nm (top panel) and 976-to-542 nm (bottom panel) upconversion nanoparticles, respectively. Column 1 shows the bright-field image that outlines the profiles of the cells (Scale bar = 5 μm). Column 2 depicts blue images of DAPI (λ_{ex}: 365 nm, λ_{em}: 450−490 nm) that indicate the nuclear regions are shown in panel 2. Columns 3-5 are red (λ_{ex}: 808 nm, λ_{em}: 650−680 nm) and green (λ_{ex}: 980 nm, λ_{em}: 530−560 nm) upconversion luminescence images obtained in the presence of pork muscle tissues of varying thickness.

analysis (Figure 2e). All the XRD peaks were well indexed in accordance with the standard pattern of β-$NaGdF_4$ (JCPDS. no. 27-0699), confirming the formation of pure hexagonal phase $NaLnF_4$ nanoparticles without noticeable cubic phase impurities, which is often detected for $NaLnF_4$ nanoparticles composed of heavy lanthanide elements.[10]

We then optimized the inner shell composition for promoting the 660-nm upconversion emission. Er^{3+} ions typically display several emission peaks centered at 408 nm, 526 nm, 542 nm, and 660 nm, corresponding to $^2H_{9/2} \rightarrow {}^4I_{15/2}$, $^2H_{11/2} \rightarrow {}^4I_{15/2}$, $^4S_{3/2} \rightarrow {}^4I_{15/2}$, and $^4F_{9/2} \rightarrow {}^4I_{15/2}$ transitions of Er^{3+}, respectively. The relative intensity of the multi-peak emission was manipulated by controlling the back-energy-transfer from Er^{3+} to Yb^{3+} through control of Yb^{3+} concentration (Figure 3a). We have assessed a series of $NaYbF_4$:Nd@$NaGdF_4$:Yb/Er@$NaGdF_4$ nanoparticles with varying Yb^{3+} concentrations in the inner shell layer (Figure S4). As shown in Figure 3b, the red emission of Er^{3+} gradually dominated the spectra with increasing Yb^{3+} concentration from 18 to 78 mol %, which corresponds to intensity ratios of red-to-green emission from 0.5 to 0.7, 0.85 and 1.9. The steady increase in red-to-green emission intensity ratio was mainly induced by the $^4S_{3/2} + {}^2F_{7/2} \rightarrow {}^4I_{13/2} + {}^2F_{5/2}$ and $^4I_{13/2} + {}^2F_{5/2} \rightarrow {}^4F_{9/2} + {}^2F_{7/2}$ cross-relaxations at elevated Yb^{3+} concentrations.[11] Further increasing Yb^{3+} concentration didn't lead to noticeable improvement in red emission of Er^{3+}, probably due to the poor shell quality as a result of fast shell deposition process in the absence of Gd^{3+} cofactors (Figure S5). We also examined relevant nanoparticles comprising high concentrations of Er^{3+} in the inner shell layer, which are known to induce $^4S_{3/2} + {}^4I_{9/2} \rightarrow {}^4F_{9/2} + {}^4F_{9/2}$ cross-relaxation between Er^{3+} ions for promoting the red emission of Er^{3+}.[11a] Photoluminescence investigation showed that the emission spectra of Er^{3+} can only be marginally tuned by varying Er^{3+} concentration, accompanied by a decrease in overall emission intensity at high Er^{3+} contents (Figure S6). Taken together, the optimal Yb/Er concentration were determined to be 78/2 mol %.

The as-synthesized nanoparticles can be readily transferred to aqueous solutions with high colloidal stability and biocompatibility by ligand exchange with 2-aminoethyl dihydrogen phosphates (AEP) or poly(acrylic acid) (PAA) (Figure S7). The zeta potential and mean effective diameter of the PAA-capped nanoparticle were measured to be -29.3 mV and 65 nm, respectively. The cell viability remained above 88 % in the presence of a high concentration of the nanoparticles (up to 500 μg/mL) (Figure 4). Importantly, the upconversion profile in aqueous solutions closely resembles that in organic solvents owing to the $NaGdF_4$ protection shell, which offers promising opportunities for deep tissue labeling.

We first demonstrated that the core−shell−shell nanoparticles are useful for specific detection of tumor cells in tissue environment. *KB cells* overexpressed with folic acid receptor were chosen as model cells for the imaging study. To achieve specific cell recognition, the nanoparticles were conjugated with folic acid (FA) (Figure S7) before incubation with the cells at 37 °C for 4 hours. The cells were then examined with luminescence microscopy, revealing clear red upconversion emission from Er^{3+} upon 808-nm excitation (Figure 5). We also recorded bright-field and blue channel images showing the profiles of *KB cells* and the location of the 4, 6-diamidino-2-phenylindole (DAPI)-stained cell nuclei. The red-channel, blue-channel, and bright-field images together unambiguously confirmed that the red signal of Er^{3+} was originated from FA-conjugated nanoparticles endocytosed by the *KB cells*. By contrast, no upconversion emission was observed when *KB cells* were cultured with FA-free nanoparticles (Figure S8). These results corroborate that the folate receptors overexpressed on the surface of the *KB cells* facilitate the recognition of the FA-conjugated nanoparticles and induce the preferential uptake of the nanoconjugates by receptor-mediated endocytosis.[12] Importantly, the optical emission can be clearly observed when a 5-mm pork muscle tissue is placed between the cells and the irradiating laser. The upconversion emission signals were still detectable after the thickness of the pork muscle tissue was increased to 10 mm. As an control experiment, we also carried out parallel detection studies by using classical $NaYF_4$:Yb/Er (18/2 mol %)@$NaYF_4$ core−shell nanoparticles (Figure S9) that efficiently upconvert 976-nm laser

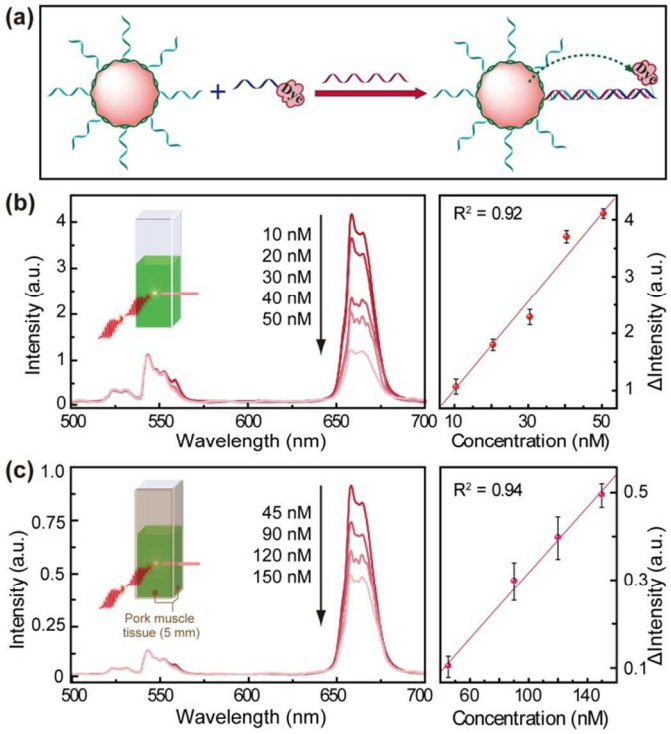

Fig. 6 DNA detection with the upconversion nanoparticles. (a) Schematic design of using the upconversion nanoparticle as LRET-based sensor system for DNA detection. (b, c) DNA detection with the core-shell-shell nanoparticles in a standard *in vitro* assay format and in the presence of tissue interference, respectively. The circlets in the calibration curves are variations in intensity of the relevant emission peaks in the presence of the analyte. Error bars shown represent the standard deviations from five repeated measurements..

irradiations. As shown in the bottom panel of Figure 5, these nanoparticles can hardly be detected when the laser beam is blocked by a pork muscle tissue as thin as 5 mm. The comparison clearly indicates higher tissue penetration depth offered by the core−shell −shell nanoprobes that can be excited by 808-nm laser.

The dominant far-red emission by 808-nm excitation offered by the core−shell−shell nanoparticles is also advantageous for accurate detection of biomolecules by means of spectroscopy, which are essential for pathological study and early diagnosis of diseases.[13] As a proof of concept, we constructed a luminescence resonance energy transfer (LRET)-based biosensor to show sensitive DNA detection. As illustrated in Figure 6a, the DNA-sensor adopts a sandwich-type hybridization format that involves two short oligonucleotides to capture a longer target oligonucleotide. One short oligonucleotide (5′-AAC TGA TGC TG -C3-NH_2-3′, denoted as capture-DNA) was modified with amine group on the 3' to conjugate with the PAA-functionalized upconversion nanoparticles (Figures S10-11). Another short oligonucleotide (5′-Cy5-C3-AGG GTT TCA GA-3′, denoted as reporter-DNA) was labeled with Cy5 on the 5' whose excitation spectrum largely coincides with the red emission band of the upconversion nanoparticles at 660 nm (Figure S12). We thereby took the advantage of our engineered core−shell−shell nanoparticles with extensive emission in the first biological spectral window to facilitate the LRET process for DNA detection. The target sequence (5′-CAG CAT CAG TTT CTG AAA CCC T-3′, denoted as target-DNA) is one genetic marker of spinal muscular atrophy, a childhood neuromuscular disease characterized by the loss of α-motor neurons leading to symmetrical wasting of the voluntary muscles.[14]

The performance of the DNA-sensor was first evaluated in a standard *in vitro* assay. Upon 808-nm excitation, the mixture of capture-DNA-conjugated upconversion nanoparticles (0.1 mg/mL) and the reporter-DNA (1.0 μM) shows only signals from the upconversion nanoparticles, in contrast to sensor systems using quantum dots or organic dyes as donors that typically suffer from interference of autofluorescence from acceptors.[15] Upon addition of the target-DNA, the red emission band of the upconversion nanoparticles in the 650−680 nm range declined significantly with respect to the green emission band in the range of 514 to 560 nm (Figure 6b, left panel). The results indicated clear energy transfer from the red-emitting Er^{3+} to the Cy5, owing to the formation of DNA duplexes that brings the Cy5 fluorophore (energy acceptor) and the upconversion nanoparticle (energy donor) into close proximity. In addition, the intensity of red emission band of Er^{3+} was found to decline linearly with the concentration of the target-DNA increasing from 10 to 50 nM (Figures 6b), along with an enhanced acceptor emission (Figure S13) as observed in previous reports.[16] By contrast, the donor emission was essentially not affected in the absence of the capture DNA under otherwise identical conditions (Figure S14). The observation further confirms the dominant role of nonradiative interaction in the energy transfer process that is strongly dependent on the donor-acceptor separations. The detection limit of the assay, corresponding to an analyte concentration that provides a signal intensity being three times the standard deviation above the signal of the control experiments, was estimated to be 5.4 nM. The DNA-sensor is highly selective to target-DNAs. The sensor response is essentially unaffected by interference DNA strands of random sequences and BSA (Figure S15). Notably, by adapting formamide to tune the stringency of the hybridization, the method can offer appreciable selectivity for single-nucleotide polymorphism characterized by single-base mismatch (Figure S16).

To shed light on its promise for potential *in vivo* studies, the DNA-sensor was enveloped in a pork muscle tissue of 5-mm thick to mimic the environment of *in vivo* detection that typically suffers from serious light absorption and scattering by the surrounding tissues (Figure 6c). As anticipated, we observed a similar spectral response to the target-DNA. The detection limit is evaluated to be 32 nM, as an increased nanoparticle concentration (0.5 mg/mL) is needed to provide sufficient signal strength to penetrate through the covered pork muscle tissue. The successful DNA detection in tissue environment by using the core−shell−shell nanoparticles is attributed to the high transparency of tissues to light emission within the first biological window, which is supported by the increased red-to-green intensity ratio of Er^{3+} (2.5 fold) when the pork muscle tissue is inserted. For comparison, we also built a DNA-sensor comprising $NaYF_4$:Yb/Er (18/2 mol %)@$NaYF_4$ core−shell nanoparticle that generates 976-to-542 nm upconversion as energy donor coupled with Cy3 as acceptor. Under comparable experimental settings (i.e.; nanoparticle concentration and laser power density), we can hardly record acceptable signal-to-noise ratio with 976-nm excitation in the control experiment, albeit an appreciably low detection limit (4.6 nM) can be achieved in a standard *in vitro* assay in the absence of pork tissue wrapping (Figure S17). The results are largely owing to stronger attenuation of 976 nm than 808 nm laser radiations by pork tissues, which further substantiates the prospective of our core−shell−shell nanoparticle bioprobes for *in vivo* bioimaging and biodetection.

Conclusions

We have developed upconversion bioprobes with excitation and emission both located in the first biological window, based on precise control over energy exchange interactions among Nd^{3+}, Yb^{3+}, and Er^{3+} in a core−shell−shell nanostructure. These bioprobes offer sensitive detection at cellular and molecular levels, registering an un-optimized detection limit of 5.4 nM. Due to largely minimized absorption of the excitation and emission light by water and hemoglobin in biological samples, the probes also enable cellular and molecular detections in the presence of tissue (5 mm) wrapping. By varying the surface modification, the core−shell−shell nanoparticles presented here are expected to provide promising alternatives to conventional bioprobes for theranostic applications.

Experimental Section

Synthesis of the core nanoparticles: The nanoparticles synthesis was developed via a modified wet chemical procedure.[8] In a typical procedure to the synthesis of $NaYbF_4$:Nd nanoparticles, 2-mL water solution of $Ln(CH_3CO_2)_3$ (0.2 M, Ln = Yb and Nd) was added to a 50-mL flask containing 4 mL of oleic acid and 6 mL of 1-octadecene. The mixture was heated at 160 °C for 40 min to form the lanthanide-oleate complexes and then cooled down to 50 °C naturally. Thereafter, 5 mL of methanol solution containing NH_4F (1.55 mmol) and NaOH (1 mmol) was added and the resultant solution was stirred for 30 min. After the methanol was evaporated, the solution was heated to 290 °C under argon for 1 h and then cooled down to room temperature. The resulting nanoparticles were precipitated by the addition of ethanol, collected by centrifugation at 6000 rpm for 5 min, washed with ethanol several times, and re-dispersed in 4 mL of cyclohexane.

General procedure for epitaxial growth of the shell layers: The shell precursor was first prepared by mixing 2-mL water solution of corresponding lanthanide acetates (0.2 M) with 4mL of oleic acid and 6 mL of 1-octadecene in a 50-mL flask followed by heating at 160 °C for 40 min. After cooling down to 50 °C, preformed core nanoparticles dispersed in 4 mL of cyclohexane were added along with a 5-mL methanol solution of NH_4F (1.55 mmol) and NaOH (1 mmol). The resulting mixture was stirred at 50 °C for 30 min, at which time the solution was heated to 290 °C under argon for 1 h and then cooled down to room temperature. The resulting nanoparticles were precipitated by the addition of ethanol, collected by centrifugation at 6000 rpm for 5 min, washed with ethanol several times, and re-dispersed in 4 mL of cyclohexane. The procedures were repeated for layer-by-layer growth of multishell nanoparticles.

Surface Modification of nanoparticles: The as-synthesized nanoparticles that are capped with oleate ligands were surface modified by using a general ligand exchange procedure. Typically, 15 mL of diethylene glycol solution containing 0.5 g of poly(acrylic acid) (PAA, MW≈1800) was heated to 110 °C with vigorous stirring under argon flow. A cyclohexane solution (10 mL) containing the nanoparticles (0.5 mmol) was injected into the hot solution, which was then heated to 240 °C and kept at this temperature for 30 min under argon flow. After the solution was cooled to room temperature, 1 mL of dilute hydrochloric aqueous solution (0.10 M) was added to precipitate the PAA-capped nanoparticles. The precipitates were collected by centrifugation, washed several times with deionized (DI) water, neutralized with a dilute solution of NaOH (0.01 M), and finally re-dispersed in PBS buffer (pH = 7.4).

Cytotoxicity of surface-functionalized core−shell−shell nanoparticles: *KB cells* were seeded in 96-well plates at a density of 2,000 cells/well and cultured in 5% CO_2 at 37 °C for 72 h. Then the cells were treated with different concentrations of nanoparticles and incubated for 24 h. The cytotoxicity was evaluated by assessing the cell viability through the 3-(4,5-dimethylthiazol-2-yl)-5-(3-carboxymethoxyphenyl)-2-(4-sulfophenyl)-2H-tetrazolium (MTS) assay (Figure S7).

Synthesis of DNA–conjugated core−shell−shell nanoparticles: The bioconjugation of DNA with the PAA-capped nanoparticles was conducted in the assistance of 1-Ethyl-3-(3-dimethylaminopropyl)carbodiimide (EDC) (Figure S11). Typically, 1 mL of the PAA-capped core−shell−shell nanoparticle dispersion (1 mg/mL) was mixed with 1 μmol capture-DNA and 1 μmol EDC, followed by incubation for 24 hours at room temperature. The nanoconjugates were separated by centrifugation after adding excess ethanol. The precipitate was re-dispersed in Tris-HCl buffer (pH = 7.4) and centrifuged with ethanol twice to remove unreacted DNA and EDC. The obtained precipitates composed of the capture-DNA-conjugated nanoparticles were dispersed in 1 mL Tris-HCl buffer (pH = 7.4) for subsequent use in hybridization assays.

Synthesis of folic acid–conjugated core−shell−shell nanoparticles: Covalent conjugation of folic acid (FA) to AEP-capped core−shell−shell nanoparticles was conducted by using a modified EDC-NHS reaction. In a typical procedure, 15 mg of FA was first dissolved in 20 mL PBS (pH 7.4). Then 0.4 mM EDC and 0.4 mM NHS were added to activate the carboxyl groups of FA for 3 h. Thereafter, 10 mg of AEP-capped core−shell−shell nanoparticles were added and the resultant mixture was allowed to react at room temperature for 12 h. The obtained FA-conjuageted core−shell−shell nanoparticles were purified with PBS and ethanol to remove unreacted chemicals by centrifugation. The linkage of folic acid with the nanoparticles was confirmed by FTIR spectra (Figure S6)

Cell culture and optical microscopy: *KB cells* were cultured in folic acid (FA)-free RPMI-1640 medium (Gibco) supplemented with 10% (v/v) fetal bovine serum and 50 units/mL penicillin/streptomycin at 37 °C under humidified air containing 5% CO_2. The cells were seeded onto glass slides and allowed to adhere for 40 h. The cells were incubated in fresh medium containing 100 μg/mL nanoparticles for 4 h under 5% CO_2 and then washed three times with PBS to sufficiently remove excess nanoparticles. Cell nuclei were subsequently stained by 4',6-diamidino-2-phenylindole (DAPI) at 37 °C for 5 min and washed with PBS. The cell imaging was performed on Olympus 1X81 microscope with the excitation light adapted to a 808-nm diode laser.

Nanoparticle imaging in tissue: PAA-capped core−shell−shell (1 mg mL^{-1}) and $NaYF_4$:Yb/Er (18/2 mol %)@$NaYF_4$ nanoparticles (1 mg/mL) were first dropped on a glass slide with capillary tubes to form a round drop. After evaporation of the solvent, the two sides of glass slide with the spot of nanoparticles were covered by pork muscle tissues and irradiated by 808 and 976 nm diode lasers, respectively. Upconversion luminescence images were recorded at the opposite side of the laser.

Target-DNA detection with the capture-DNA–conjugated nanoparticles: 0.1 mL of the capture-DNA-nanoparticle conjugates (0.1 mg/mL) was mixed with 0.1 mL of reporter-DNA (labeled with Cy5, 1.0 μM) and stirred for 10 minutes. Then 0.1 mL of target-DNA of different concentrations was added. After incubation for 1 hour, the resultant mixture was subjected to examination through upconversion luminescence spectroscopy by 808-nm laser excitation. For the DNA detection in the presence of tissue wrapping, the concentration of core−shell−shell nanoparticle-capture-DNA conjugates and reporter-DNA were increased to 0.5 mg/mL and 5.0 μM, respectively, for the purpose of enhancing the emission intensity to penetrate through the pork muscle tissue. For control experiment that uses the $NaYF_4$:Yb/Er (18/2 mol %)@$NaYF_4$ core−shell nanoparticles, the experimental setup is identical except that the reporter-DNA is labeled with Cy3 to match the green emission band of Er^{3+}.

Characterizations: Transmission electron microscopy (TEM) images were carried out on a Philips CM-20 transmission electron microscope operating at an acceleration voltage of 200 kV. Powder X-ray diffraction (XRD) pattern was collected on a BRUKER AXS D2 Phaser X-ray diffractometer with Cu Kα1 radiation (λ = 0.154 nm). The infrared spectra were recorded on a PerkinElmer Spectrum 100 Fourier-transform infrared spectrometer (FTIR). Ultraviolet-visible absorption spectra were acquired on a SHIMADZU UV-1700 PharmaSpec UV-Vis spectrophotometer. Photoluminescence spectra were recorded at room temperature with an F-4600 spectrophotometer (Hitachi) with the excitation source adapted to fiber coupled diode lasers. Unless otherwise stated, all spectra were obtained from cyclohexane dispersion of nanoparticles (1 wt %) at an excitation power density of 15 W/cm^2. Luminescence digital photographs were taken with a Nikon D90 camera. Optical microscopy imaging was performed on an Olympus 1X81 microscope with the xenon lamp adapted to a diode laser. The excitation source was a 808/980 nm laser, which directly irradiated on the cell (or pork when the cells were covered) and the diameter of the laser beam was expanded to ~1.0 cm. Two D660/20x (for red) and D545/40x (for green) emission filters were used for bioimaging Micrographs were recorded with a micro manager imaging system.

Acknowledgements

This work was supported by City University of Hong Kong (Nos. 7200317 and 9610257) and National Natural Science Foundation of China (Nos. 21303149, 51332008, and 21371145). We thank Mr. Wei Li for the help on optical microscopy.

Notes and references

[a]Department of Physics and Materials Science, City University of Hong Kong, 83 Tat Chee Avenue, Hong Kong SAR (China)
[b]Department of Biology and Chemistry, City University of Hong Kong, 83 Tat Chee Avenue, Hong Kong SAR (China)
[c]Department of Medical and Biomedical Engineering, City University of Hong Kong, 83 Tat Chee Avenue, Hong Kong SAR (China)
[d]City University of Hong Kong Shenzhen Research Institute, Shenzhen 518057, China.
*To whom correspondence should be addressed. E-mail: fwang24@cityu.edu.hk

Electronic Supplementary Information (ESI) available: [details of any supplementary information available should be included here]. See DOI: 10.1039/b000000x/

1 a) Y. Weizmann, Z. Cheglakov, V. Pavlov and I. Willner, *Angew. Chem. Int. Ed.* 2006, **45**, 2238; b) J. H. Yu, S.-H. Kwon, Z. Petrášek, O. K. Park, S. W. Jun, K. Shin, M. Choi, Y. I. Park, K. Park, H. B. Na, N. Lee, D. W. Lee, J. H. Kim, P. Schwille and T. Hyeon, *Nat. Mater.* 2013, **12**, 359; c) L. Y. Feng, L. Wu and X. G. Qu, *Adv. Mater.* 2013, **25**, 168; d) P. Zhang, T. Beck and W. H. Tan, *Angew. Chem. Int. Ed.* 2001, **40**, 402; e) Y. Xiang, A. J. Tong and Y. Lu, *J. Am. Chem. Soc.* 2009, **131**, 15352; f) G. Z. Zhu, J. Zheng, E. Q. Song, M. Donovan, K. J. Zhang, C. Liu and W. H. Tan, *Proc. Natl. Acad. Sci. U.S.A.* 2013, **110**.
2 a) G. Y. Chen, T. Y. Ohulchanskyy, A. Kachynski, H. Agren and P. N. Prasad, *ACS Nano* 2011, **5**, 4981; b) G. S. Hong, J. C. Lee, J. T. Robinson, U. Raaz, L. M. Xie, N. F. Huang, J. P. Cooke and H. J. Dai, *Nat. Med.* 2012, **18**, 1841; c) M. Nyk, R. Kumar, T. Y. Ohulchanskyy, E. J. Bergey and P. N. Prasad, *Nano. Lett.* 2008, **8**, 3834; d) J. Wang, F. Wang, C. Wang, Z. Liu and X. G. Liu, *Angew. Chem. Int. Ed.* 2011, **50**, 10369; e) U. Rocha, K. U. Kumar, C. Jacinto, I. Villa, F. Sanz-Rodríguez, M. del Carmen Iglesias de la Cruz, A. Juarranz, E. Carrasco, F. C. J. M. van Veggel, E. Bovero, J. G. Solé and D. Jaque, *Small* 2014, **10**, 1141; f) N. N. Dong, M. Pedroni, F. Piccinelli, G. Conti, A. Sbarbati, J. E. Ramirez-Hernandez, L. M. Maestro, M. C. Iglesias-de la Cruz, F. Sanz-Rodriguez, A. Juarranz, F. Chen, F. Vetrone, J. A. Capobianco, J. G. Sole, M. Bettinelli, D. Jaque and A. Speghini, *ACS Nano* 2011, **5**, 8665; g) L. M. Maestro, J. E. Ramirez-Hernandez, N. Bogdan, J. A. Capobianco, F. Vetrone, J. G. Sole and D. Jaque, *Nanoscale* 2012, **4**, 298.
3 a) J. Zhou, Z. Liu and F. Y. Li, *Chem. Soc. Rev.* 2012, **41**, 1323; b) X. C. Ye, J. Chen, M. Engel, J. A. Millan, W. B. Li, L. Qi, G. Z. Xing, J. E. Collins, C. R. Kagan, J. Li, S. C. Glotzer and C. B. Murray, *Nat. Chem.* 2013, **5**, 466; c) P. Huang, J. Lin, W. W. Li, P. F. Rong, Z. Wang, S. J. Wang, X. P. Wang, X. L. Sun, M. Aronova, G. Niu, R. D. Leapman, Z. H. Nie and X. Y. Chen, *Angew. Chem. Int. Ed.* 2013, **52**, 13958; d) Q. Yuan, Y. Wu, J. Wang, D. Q. Lu, Z. L. Zhao, T. Liu, X. B. Zhang and W. H. Tan, *Angew. Chem. Int. Ed.* 2013, **52**, 13965; e) H. S. Qian, H. C. Guo, P. C. L. Ho, R. Mahendran and Y. Zhang, *Small* 2009, **5**, 2285; f) Y. Q. Lu, J. Lu, J. B. Zhao, J. Cusido, F. M. Raymo, J. L. Yuan, S. Yang, R. C. Leif, Y. J. Huo, J. A. Piper, J. P. Robinson, E. M. Goldys and D. Y. Jin, *Nat. Commun.* 2014, **5**, Doi 10.1038/Ncomms4741; g) D. J. Gargas, E. M. Chan, A. D. Ostrowski, S. Aloni, M. V. P. Altoe, E. S. Barnard, B. Sanii, J. J. Urban, D. J. Milliron, B. E. Cohen and P. J. Schuck, *Nat. Nanotechnol.* 2014, **9**, 300; h) G. F. Wang, Q. Peng and Y. D. Li, *Accounts. Chem. Res.* 2011, **44**, 322; i) N. Bogdan, F. Vetrone, G. A. Ozin and J. A. Capobianco, *Nano. Lett.* 2011, **11**, 835.
4 a) F. van de Rijke, H. Zijlmans, S. Li, T. Vail, A. K. Raap, R. S. Niedbala and H. J. Tanke, *Nat. Biotechnol.* 2001, **19**, 273; b) Y. I. Park, J. H. Kim, K. T. Lee, K.-S. Jeon, H. B. Na, J. H. Yu, H. M. Kim, N. Lee, S. H. Choi, S.-I. Baik, H. Kim, S. P. Park, B.-J. Park, Y. W. Kim, S. H. Lee, S.-Y. Yoon, I. C. Song, W. K. Moon, Y. D. Suh and T. Hyeon, *Adv. Mater.* 2009, **21**, 4467; c) F. Wang, R. R. Deng, J. Wang, Q. X. Wang, Y. Han, H. M. Zhu, X. Y. Chen and X. G. Liu, *Nat. Mater.* 2011, **10**, 968; d) Y. Q. Lu, J. B. Zhao, R. Zhang, Y. J. Liu, D. M. Liu, E. M. Goldys, X. S. Yang, P. Xi, A. Sunna, J. Lu, Y. Shi, R. C. Leif, Y. J. Huo, J. Shen, J. A. Piper, J. P. Robinson and D. Y. Jin, *Nat. Photonics.* 2014, **8**, 33; e) Q. Liu, W. Feng, T. S. Yang, T. Yi and F. Y. Li, *Nat. Protoc.* 2013, **8**, 2033; f) M. Haase and H. Schäfer, *Angew. Chem. Int. Ed.* 2011, **50**, 5808; g) X. Li, R. Wang, F. Zhang and D. Zhao, *Nano Lett.* 2014, **14**, 3634; h) D. L. Ni, J. W. Zhang, W. B. Bu, H. Y. Xing, F. Han, Q. F. Xiao, Z. W. Yao, F. Chen, Q. J. He, J. N. Liu, S. J. Zhang, W. P. Fan, L. P. Zhou, W. J. Peng and J. L. Shi, *ACS Nano* 2014, **8**, 1231; i) J. N. Liu, Y. Liu, W. B. Bu, J. W. Bu, Y. Sun, J. L.

Du and J. L. Shi, *J. Am. Chem. Soc.* 2014, **136**, 9701; j) Z. J. Gu, L. Yan, G. Tian, S. J. Li, Z. F. Chai and Y. L. Zhao, *Adv. Mater.* 2013, **25**, 3758.
5 a) P. Pantazis, J. Maloney, D. Wu and S. E. Fraser, *Proc. Natl. Acad. Sci. USA* 2010, **107**, 14535; b) D. M. Yang, Y. L. Dai, J. H. Liu, Y. Zhou, Y. Y. Chen, C. X. Li, P. A. Ma and J. Lin, *Biomaterials* 2014, **35**, 2011.
6 a) X. Chen, D. Peng, Q. Ju and F. Wang, *Chem. Soc. Rev.* 2015, **44**, 1318; b) P. Kannan, F. Abdul Rahim, R. Chen, X. Teng, L. Huang, H. Sun and D.-H. Kim, *ACS Appl. Mater. Interfaces* 2013, **5**, 3508.
7 a) Y. F. Wang, G. Y. Liu, L. D. Sun, J. W. Xiao, J. C. Zhou and C. H. Yan, *ACS Nano* 2013, **7**, 7200; b) H. Wen, H. Zhu, X. Chen, T. F. Hung, B. Wang, G. Zhu, S. F. Yu and F. Wang, *Angew. Chem. Int. Ed.* 2013, **52**, 13419; c) X. J. Xie, N. Y. Gao, R. R. Deng, Q. Sun, Q. H. Xu and X. G. Liu, *J. Am. Chem. Soc.* 2013, **135**, 12608; d) E. Hemmer, N. Venkatachalam, H. Hyodo, A. Hattori, Y. Ebina, H. Kishimoto and K. Soga, *Nanoscale* 2013, **5**, 11339; e) Y. Zhong, G. Tian, Z. Gu, Y. Yang, L. Gu, Y. Zhao, Y. Ma and J. Yao, *Adv. Mater.* 2014, **26**, 2831; f) X. Li, R. Wang, F. Zhang, L. Zhou, D. Shen, C. Yao and D. Zhao, *Sci. Rep.* 2013, **3**, 3536.
8 F. Wang, R. Deng and X. Liu, *Nat. Protoc.* 2014, **9**, 1634.
9 K. E. Sapsford, L. Berti and I. L. Medintz, *Angew. Chem. Int. Ed.* 2006, **45**, 4562.
10 Q. Liu, Y. Sun, T. Yang, W. Feng, C. Li and F. Li, *J. Am. Chem. Soc.* 2011, **133**, 17122.
11 a) J. Yang, C. M. Zhang, C. Peng, C. X. Li, L. L. Wang, R. T. Chai and J. Lin, *Chem. Eur. J.* 2009, **15**, 4649; b) F. Vetrone, J. C. Boyer, J. A. Capobianco, A. Speghini and M. Bettinelli, *J. Appl. Phys.* 2004, **96**, 661; c) A. Punjabi, X. Wu, A. Tokatli-Apollon, M. El-Rifai, H. Lee, Y. Zhang, C. Wang, Z. Liu, E. M. Chan, C. Duan and G. Han, *ACS Nano* 2014, **8**, 10621.
12 a) Y. Choi, S. Kim, M.-H. Choi, S.-R. Ryoo, J. Park, D.-H. Min and B.-S. Kim, *Adv. Funct. Mater.* 2014, **24**, 5781; b) L.-S. Wang, L.-C. Wu, S.-Y. Lu, L.-L. Chang, I. T. Teng, C.-M. Yang and J.-a. A. Ho, *ACS Nano* 2010, **4**, 4371.
13 a) W. Farris, S. Mansourian, Y. Chang, L. Lindsley, E. A. Eckman, M. P. Frosch, C. B. Eckman, R. E. Tanzi, D. J. Selkoe and S. Guénette, *Proc. Natl. Acad. Sci. USA* 2003, **100**, 4162; b) D. Razansky, M. Distel, C. Vinegoni, R. Ma, N. Perrimon, R. W. Koster and V. Ntziachristos, *Nat. Photon.* 2009, **3**, 412.
14 Q. Ju, U. Uddayasankar and U. Krull, *Small* 2014, **10**, 3912.
15 a) Z. G. Chen, H. L. Chen, H. Hu, M. X. Yu, F. Y. Li, Q. Zhang, Z. G. Zhou, T. Yi and C. H. Huang, *J. Am. Chem. Soc.* 2008, **130**, 3023; b) W. Zheng, P. Huang, D. Tu, E. Ma, H. Zhu and X. Chen, *Chem. Soc. Rev.* 2015, **44**, 1379.
16 a) Q. Liu, B. R. Yin, T. S. Yang, Y. C. Yang, Z. Shen, P. Yao and F. Y. Li, *J. Am. Chem. Soc.* 2013, **135**, 5029; b) D. E. Achatz, R. J. Meier, L. H. Fischer and O. S. Wolfbeis, *Angew. Chem. Int. Ed.* 2011, **50**, 260; c) M. Y. He and Z. H. Liu, *Anal. Chem.* 2013, **85**, 11691; d) H. Li and L. Y. Wang, *Analyst* 2013, **138**, 1589; e) P. Zhang, S. Rogelj, K. Nguyen and D. Wheeler, *J. Am. Chem. Soc.* 2006, **128**, 12410; f) X. Hu, T. Wei, J. Wang, Z.-E. Liu, X. Li, B. Zhang, Z. Li, L. Li and Q. Yuan, *Anal. Chem.* 2014, **86**, 10484.